Mo Single Atoms Modified Ru Nanoparticles Assemblies for Hydrogen Evolution Reaction in Seawater Electrocatalysis

Shuhan Wang , Jiani Qin * , Yong Zhang , Shuai Chen , Wenjun Yan , Haiqing Zhou , Xiujun Fan *

Posted Date: 21 March 2025

doi: 10.20944/preprints202503.1578.v1

Keywords: Hydrogen evolution reaction (HER); Bidentate ligand; Hexagonal octahedral configuration; Nanoparticle; Single atom

 doi:10.20944/preprints202503.1578.v1

Article

Mo Single Atoms Modified Ru Nanoparticles Assemblies for Hydrogen Evolution Reaction in Seawater Electrocatalysis

Shuhan Wang [1,2], Jiani Qin [1,*], Yong Zhang [3], Shuai Chen [4], Wenjun Yan [4], Haiqing Zhou [3] and Xiujun Fan [2,*]

[1] School of Environmental Science and Engineering, Shaanxi University of Science and Technology, Xi'an 710021, China

[2] School of Chemistry, Xi'an Jiaotong University, Xi'an 710049, China.

[3] Key Laboratory of Low-Dimensional Quantum Structures and Quantum Control of Ministry of Education, Department of Physics, Hunan Normal University, Changsha 410081, China

[4] State Key Laboratory of Coal Conversion, Institute of Coal Chemistry, Chinese Academy of Sciences, Taiyuan 030001, China

* Correspondence: jianiqin@sust.edu.cn (J.Q.); fxiujun@xjtu.edu.cn (X.F.)

Abstract: Ru-based catalysts manifest unparalleled hydrogen evolution reaction (HER) performance, but the hydrolysis of Ru species and the accumulation of corresponding reaction intermediates greatly limit HER activity and stability. Herein, Mo single atoms modified Ru nanoparticles assemblies supported on N-incorporated graphene (referred to as MoRu-NG) are compounded via hydrothermal and chemical vapor deposition methods (CVD). The incorporation of Mo single atoms into Ru lattices modifies the local atomic milieu around Ru centers, significantly improving HER catalytic behavior and stability. More specifically, MoRu-NG achieves the overpotential of 53 mV and 28 mV at 10 mA cm^{-2} with exceptional stability in acidic and alkaline seawater solutions, respectively. In MoRu-NG, Ru atoms have special electronic structure and thus possess optimal hydrogen adsorption energy, which indicates that the excellent HER activity mainly hinges upon Ru centers. To be specific, the d-electron orbitals of Ru atoms are close to half full, giving Ru atoms moderate bond energy for the assimilation and release of hydrogen, which is beneficial for the conversion of reaction intermediates. Moreover, the incorporation of Mo single atoms facilitates the formation of O, O'-bidentate ligands, significantly enhancing the structural stability of MoRu-NG in pH-universal seawater electrolysis. This work advances a feasible construction method of hexagonal octahedral configuration (Ru–O–Mo–N–C) and provides a route to synthesize the efficient and stable catalyst for electrocatalytic HER in pH-universal seawater.

Keywords: Hydrogen evolution reaction (HER); Bidentate ligand; Hexagonal octahedral configuration; Nanoparticle; Single atom

1. Introduction

As the emergence of low-carbon circular economy globally, hydrogen produced by water splitting is increasingly gaining attention in society. Hydrogen energy is widely regarded as an optimal medium for energy hoarding and distribution in the future, while also serving as a crucial chemical feedstock in modern industrial processes. However, due to the scarcity of freshwater resources and energy consumption associated with seawater purification, hydrogen evolution reaction (HER) may not achieve ideal effect in freshwater.

Electrocatalytic seawater splitting for hydrogen generation can not only avoid the consumption in relation to freshwater supplies in the world, but also improve the utilization rate of seawater resources. Due to its ample reserves and widespread availability, seawater is considered a latent

 doi:10.20944/preprints202503.1578.v1

feedstock for electrolysis, which results in the popularization with the purpose of producing hydrogen via seawater electrolysis [1]. In terms of catalyst section, Pt-based catalysts are considered to be effective electrocatalysts for HER, but large-scale commercialization of Pt-based catalysts faces the problem of high cost. To date, Ru-based catalysts have been regarded as one of the most up-and-coming and cheapest replacements to Pt-based catalysts for HER implementations, owing to Ru–H bond strength comparable to that of Pt–H bonds [2–6]. However, there are numerous challenges in producing hydrogen by seawater electrolysis, such as the agglomeration of Ru atoms in Ru-based catalysts and the attack of metal ions in seawater. Given the substantial binding energy of Ru atoms, irreversible agglomeration of Ru atoms occurs in the actual catalytic process, which leads to the unsatisfactory stability of Ru-based catalysts [7]. Furthermore, a large number of Cl^- and insoluble precipitates from Ca^{2+} and Mg^{2+} in seawater tend to poison catalysts, thereby reducing both HER activity and durability of catalysts [8–10]. Moreover, The innate poor conductivity of seawater and the sophisticated nature of seawater framework are not conducive to HER kinetics and poses challenges to understanding the reaction process and mechanism of seawater electrolysis [11,12]. These obstacles have contributed to the relatively slow progression of seawater electrolysis towards industrialization.

In this work, Mo single atoms modified Ru nanoparticles assemblies (Mo–Ru NPAs) supported on N-incorporated graphene (defined as MoRu-NG) are fabricated via hydrothermal and chemical vapor deposition (CVD) methods. MoRu-NG with Ru–O–Mo–N–C configuration delivers outstanding HER catalytic efficiency and stability, which surpasses those of commercial Pt/C and other reported electrocatalysts. Electron interaction exists between O and Ru sites in MoRu-NG, tuning the electronic structure of active sites to peak state and increasing the stability of O-bridged Ru-Mo structure, which facilitates HER activity and stability. Specifically, the p-band center of O sites within MoO_4^{2-} exhibits a more significant overlap with the d-band center of Ru sites, thereby improving HER activity and stability. Furthermore, O, O'-bidentate ligands in Mo–Ru NPAs are formed after the introduction of Mo single atoms (SAs), which can shorten Ru–Ru bond length in Ru nanoparticles (NPs), increasing Ru metallic bond intensity and further promoting HER stability. Importantly, the existence of Ru atoms in Mo–Ru NPAs introduces abundant acid sites of Lewis that replenish hydroxyl radicals in order to induce a negative charge accumulation, which can resist Cl^- attack in seawater. Meanwhile, these acid sites intensely bind to hydroxide ions, which prevents the pH values of seawater from rising locally, and thus inhibits the deposit formation of metal ions in the seawater [13,14]. In MoRu-NG, the characteristic Ru–O–Mo–N–C architecture with pronounced electron-pair bonds functions as a robust and top-notch catalytic structure toward HER in pH-universal seawater electrolysis.

2. Experimental

2.1. Preparation of MoRu-NG Composite

The precursors, namely $(NH_4)_6Mo_7O_{24}{\cdot}4H_2O$ and $RuCl_3{\cdot}3H_2O$, were added to aqueous suspension of GO to form a homogeneous solution. Subsequently, the resulting mixture was transferred to a Teflon-lined autoclave and heated at 180°C for 12 hours. After the heating process, the as-prepared product underwent freeze-drying, which resulted in the formation of spongy column. Sponge column of p-RGO with $RuMo_3$ groups was obtained by freeze drying of the product after hydrothermal synthesis. Last, the composite was reacted with NH_3/Ar at 800°C in CVD apparatus to obtain MoRu-NG.

2.2. Preparation of Mo-NG and Ru-NG Composites

$(NH_4)_6Mo_7O_{24}{\cdot}4H_2O$ and $RuCl_3{\cdot}3H_2O$ precursors were added to two copies of aqueous suspension of GO to form two copies of homogeneous solution, respectively. Following the same steps as 2.1, Mo-NG and Ru-NG catalysts were obtained.

 doi:10.20944/preprints202503.1578.v1

2.3. Preparation of A-MR、B-MR and C-MR Composites

Following the same steps as 2.1, A-MR、B-MR and C-MR catalysts were obtained via different atomic mass ratios.

Details are shown in the Table S1.

2.4. Materials Characterization

A JEOL-JSM-7001F SEM and JEOL 2100 field emission gun TEM were used to examine the morphology. AC HAADF-STEM images and EDS elemental mappings were carried out by a Cs-corrected FEI Titan G2 60-300 equipped with a Super-X EDS detector and operated at 300 kV. Chemical compositions and elemental oxidation states were checked by XPS spectra (PHI-5702). Raman spectra were recorded on a confocal micro-Raman spectrometer (Horiba Jobin Yvon, LabRAM HR Evolution, λ = 532 nm). N_2 adsorption–desorption isotherms were measured by a Quantachrome autosorb iQ2 analyzer. The specific area was obtained using the BET method. The pore size was calculated by the Barret-Joyner-Halenda (BJH) method. Water and air bubble CA were recorded using a DSA100 contact angle analyzer (Kruss, Germany). FT-IR spectra was collected on a Thermo Nicolet. Room-temperature EPR spectra were obtained using an EMXPLUS10/12 paramagnetic resonance spectrometer.

3. Result

3.1. Synthesis of MoRu-NG

MoRu-NG electrocatalysts were synthesized through the following steps, as portrayed in the schematic representation (**Figure 1a)**. The first step was to prepare a precursor solution using sonication Ru salt (as Ru source), molybdate (as Mo source), and graphene oxide in water. After thorough mixing, the precursor solution underwent hydrothermal treatment, in which $RuMo_3$ groups were anchored onto partially reduced GO (p-RGO), leading to the formation of Ru–O–Mo–N–C structure. After this step, freeze-drying was applied to the mixture to reduce p-RGO sheet restacking and the mixture was generated by CVD treatment in the NH_3/Ar atmosphere at 800°C.

 doi:10.20944/preprints202503.1578.v1

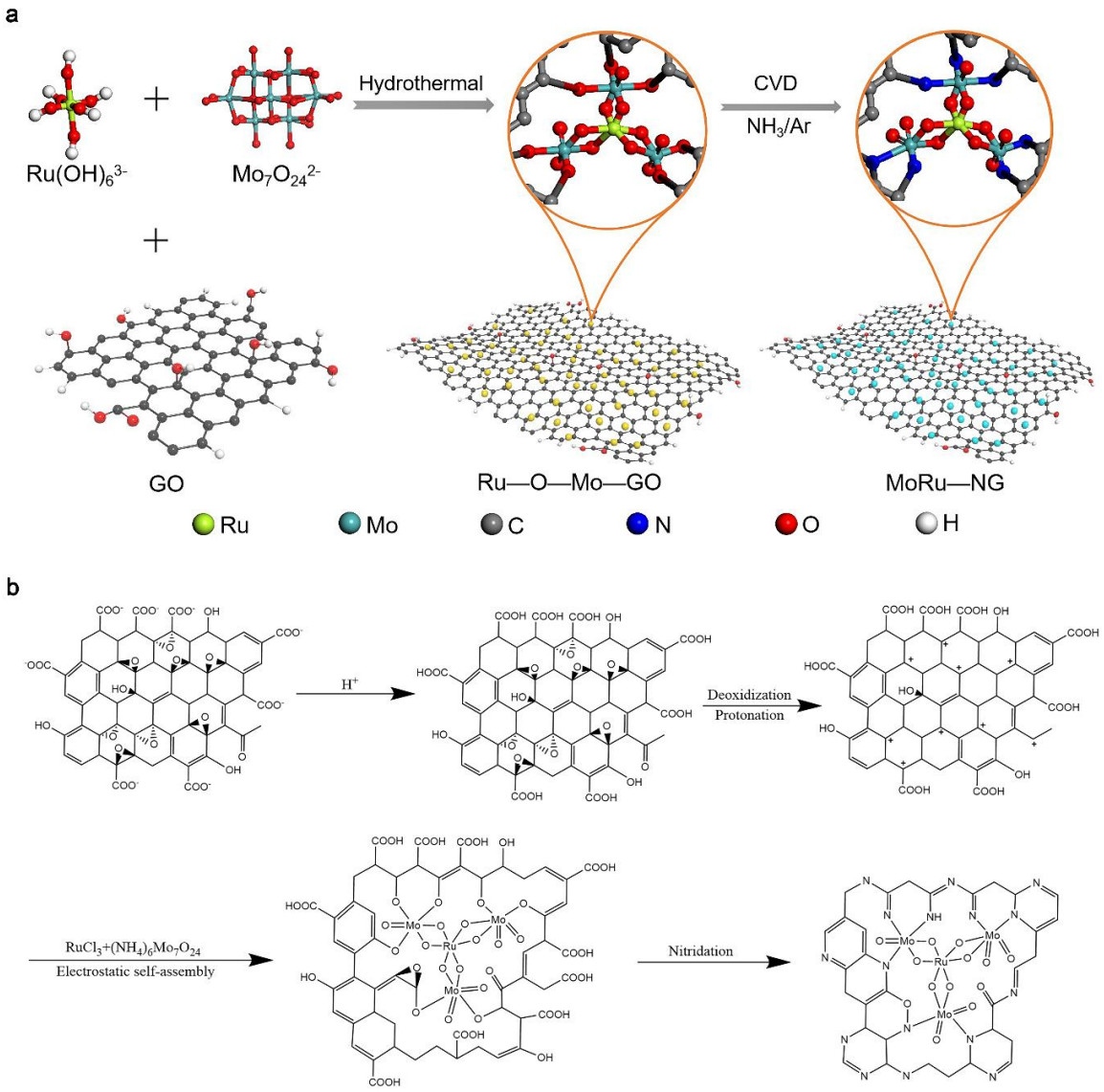

Figure 1. Synthesis of MoRu-NG. (a) Schematic illustration of the synthetic procedure. (b) The proposed chemical mechanism.

The formation mechanism of MoRu-NG electrocatalysts was based on the electrostatic self-assembly that produce intensive coupling function between Mo and Ru atoms [15,16] (**Figure 1b**). Particularly, $RuCl_3 \cdot 3H_2O$ and $(NH_4)_6Mo_7O_{24} \cdot 4H_2O$ were blended with the GO suspension inside an ultrasonic bath where the pH value ranges from 6.1 to 6.3. After that, in the course of the hydrothermal process, protonation took place for the carboxyl anions. Then the elimination of protonated carbonyl and epoxy groups on graphene oxide appeared as well as the delocalized π-electron system and H^+ underwent protonation to obtain positively charged p-RGO [17]. The p-band center of O sites in MoO_4^{2-} exhibited a more pronounced overlap with the d-band center of Ru sites, which enhanced Ru–O–Mo covalency [18]. Initially, Ru^{3+} formed aquo ligands ($[Ru(H_2O)_6]^{3+}$) in deionized water, which then underwent hydrolysis to produce $[Ru(OH)_6]^{3-}$ under high-temperature and mild acidic conditions. In a mild acidic solution simultaneously, protonation facilitated the transformation of the Mo(VI) oxo species in the MoO_4^{2-} segment. Mo(VI) oxo species firstly changed into Mo hydroxo species and ultimately evolved into Mo aquo ligands $[MoO_4(H_2O)_2]^{2-}$ [19]. $[MoO_4(H_2O)_2]^{2-}$ replaced two hydroxyl bonds in $[Ru(OH)_6]^{3-}$ to formed $[Ru(MoO_4)_3(H_2O)_6]^{3-}$ ($RuMo_3$) groups with O-bridged Ru-Mo structure, where $[MoO_4(H_2O)_2]^{2-}$ acts as O,O′-bidentate

 doi:10.20944/preprints202503.1578.v1

ligands [20]. As a result of the vigorous coupling between negatively charged $RuMo_3$ groups [15,20] and positively charged protonated p-RGO sheets, O-coordinated $RuMo_3$ groups could be electrostatically attracted onto p-RGO sheets [21,22]. During CVD process, nitrogen doping and p-RGO underwent additional reduction simultaneously, resulting in the formation of $RuMo_3$ groups anchored within p-RGO sheets, which subsequently constructed Ru–O–Mo–N–C structure. For the purpose of comparison, a sequence of composite materials with various mass percentage of Mo atoms relative to Ru atoms, together with Mo species and Ru species supported on NG severally (denoted as Mo-NG and Ru-NG, respectively), were also synthesized (**Table S1**).

The reason why MoRu-NG successful synthesis is that the interaction of coordination nature between Ru and Mo species, as well as the electronegative difference between protonated p-RGO sheets and $RuMo_3$ groups during hydrothermal process with mild acidic solution. In MoRu-NG, Ru centers possess suitable hydrogen adsorption energy and special electronic structure, which has a pivotal function in improving HER activity. Additionally, the introduction of O, O'-bidentate ligand promotes HER stability in increasing Ru metallic bond intensity [23,24].

3.2. Structural Characterization of MoRu-NG

The crystalline phase and morphology of MoRu-NG were initially investigated by X-ray diffraction (XRD), high-resolution transmission electron microscopy (HR-TEM), high-angle annular dark-field scanning TEM (HAADF-STEM), and aberration-corrected high-angle annular dark-field scanning TEM (AC HAADF-STEM).

In XRD patterns, the typical diffraction peaks of MoRu-NG reveal the presence of Ru crystalline (PDF#06-0663) phase, indicating the successful formation of Ru crystals after thermal nitridation. Additionally, no peaks related to Mo species are observed, which suggests that Mo species exist as an amorphous phase after the nitridation reaction under thermal conditions (**Figure 2a**). Notably, the diffraction peaks of MoRu-NG exhibit negative shifts relative to that of Ru/NG (selected areas in **Figure 2a**), indicating lattice expansion occurs after the introduction of Mo SAs. In addition, the XRD patterns of A-MR and C-MR also exhibit the successful formation of Ru crystals, similar to that of MoRu-NG (**Figure S1)**. As demonstrated by HR-TEM images (**Figure 2b**, **Figure S2**), Mo–Ru NPAs are homogeneous dispersion in NG sheets. In **Figure 2b** and **Figure S3**, Mo–Ru NPAs and Ru NPs with about 1.5 nm and 3.2 nm particle sizes are formed in NG sheets, respectively. This observation indicates that Mo SAs in Mo–Ru NPAs can effectively suppress the particle size of Ru-NG, leading to higher specific surface area and stronger electrical conductivity [25]. As depicted in the HR-TEM image at relatively high magnification, the lattice fringes of Mo–Ru NPAs are clear and the interplanar distance of 0.26 nm can be correlated with the (100) facets of Mo–Ru NPAs (**Figure 2c**). Additionally, the HR-TEM images of Mo-NG and Ru-NG display the state of amorphous phase and the crystal face distance of 0.24 nm corresponds to the (100) planes of Ru crystals, respectively (**Figure S4**). Moreover, lattice distortion and edge dislocation can be observed in white circles and yellow T-shape marks (**Figure 2c**, **inset**), respectively [26]. The results illustrate that introducing Mo SAs increases the specific surface area values and further exposes more active sites, improving the conductivity of MoRu-NG. After introducing Mo SAs into Ru crystal lattices, the crystal face spacing of MoRu-NG is larger than that of Ru-NG, which indicates that lattice expansion appears in MoRu-NG, consistent with the results of XRD.

 doi:10.20944/preprints202503.1578.v1

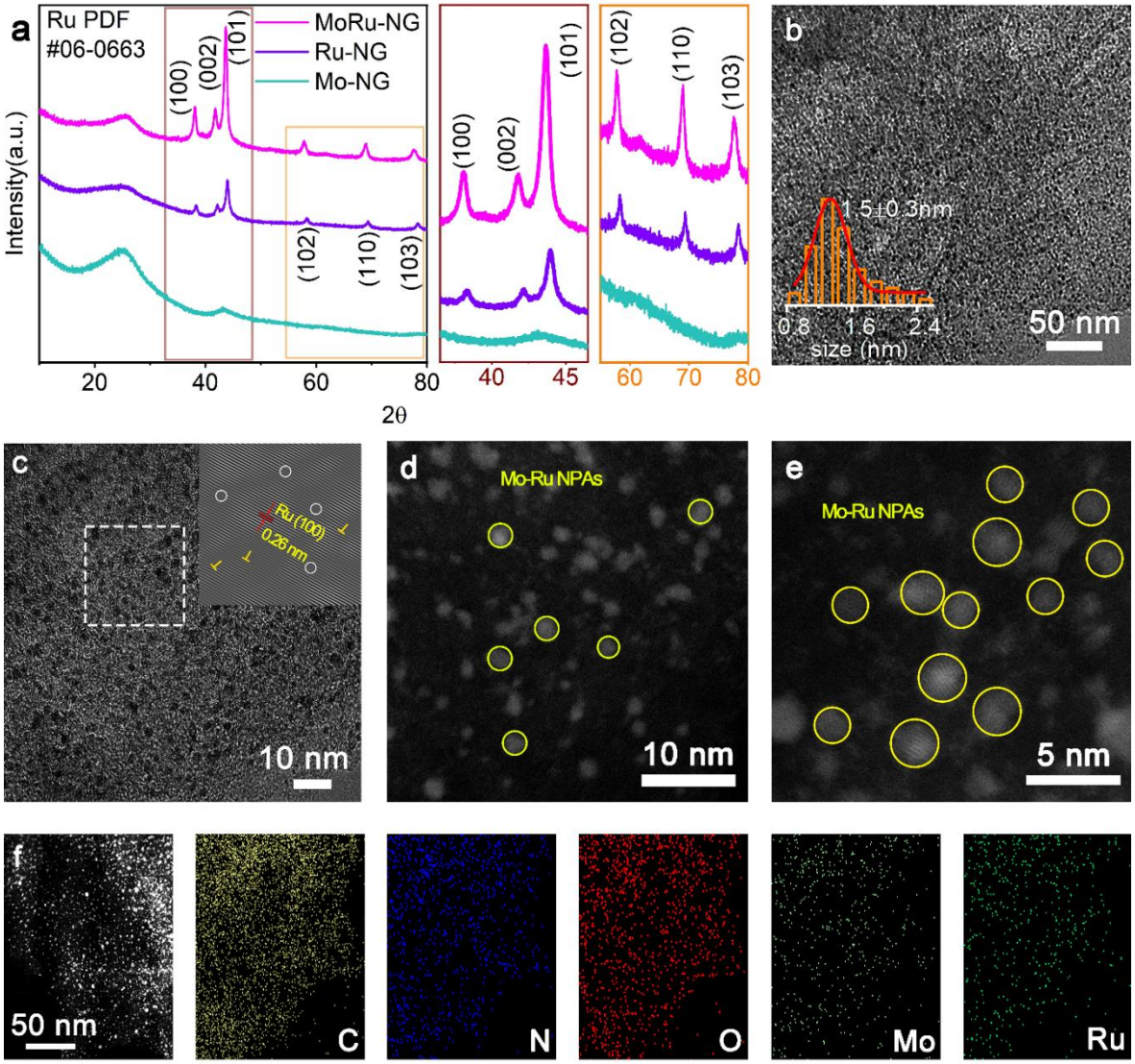

Figure 2. a) XRD patterns and selected range of XRD patterns. (b, c) HR-TEM images of MoRu-NG; inset of (b) indicates particle size distribution diagram; inset of (c) indicates lattice fringe pattern. (d, e) AC HAADF-STEM images of MoRu-NG. The image displays Mo–Ru NPAs (yellow circles). (f) HAADF-STEM image of MoRu-NG and corresponding EDS elemental mapping images.

The AC HAADF-STEM images exhibit that Mo–Ru NPAs are distributed on NG sheets, validating the interaction and electronic coupling of Mo and Ru atoms (**Figure 2d** and **Figure 2e)**. The energy-dispersive x-ray spectroscopy (EDS) mapping analysis indicates the well-distributed presence of C, N, O, Mo, and Ru elements (**Figure 2f**). The TEM-element energy dispersive spectroscopy (EDS) mapping analysis reveals that the Ru and Mo content in the synthesized Mo–Ru NPAs is close to 0.41 atom % and 0.69 atom %, respectively (**Figure S5**, **Table S2**). These findings demonstrate that densely packed Mo–Ru NPAs are effectively fabricated on NG sheets via the two methods.

To gain insights into the valence states of MoRu-NG, x-ray photoelectron spectroscopy (XPS) was carried out. The XPS survey spectrum of MoRu-NG confirms the characteristic peaks of Ru, Mo, C, N, and O species in agreement with the EDS elemental mapping (**Figure S6**, **Figure 2f**). The Mo 3d spectra of MoRu-NG exhibit three pairs of peaks, manifesting Mo(VI), Mo(V), and Mo–N species [27] (**Figure 3a**). For Ru 3p spectra of MoRu-NG, Ru species display two pairs of peaks that correspond to Ru(0) and Ru(IV), respectively [28], indicating the existence of Ru crystals on MoRu-NG surface (**Figure 3b**). Compared to control samples, positive displacements of 0.3 and 0.4 eV are

 doi:10.20944/preprints202503.1578.v1

observed on Mo(V) and Ru(0) in MoRu-NG, respectively, which demonstrates the diminution of electron density around Mo–Ru NPAs and the formation of M–O/M–N bonds (M refers to Mo/Ru). As revealed in **Figure 3c**, the deconvoluted peaks around 531.0 and 530.3 eV are assigned to Mo–O and Ru–O bonds [29–31], respectively; and the Mo–O and Ru–O bonds in MoRu-NG exhibit 0.3 eV shift toward higher binding energy relative to those of Mo-NG and Ru-NG. These results confirm that Mo–Ru NPAs are O-coordinated within MoRu-NG, indicating that the formation of Ru–O–Mo structure redistributes the Ru d-orbital electron density and affects the Mo electron cloud distribution.

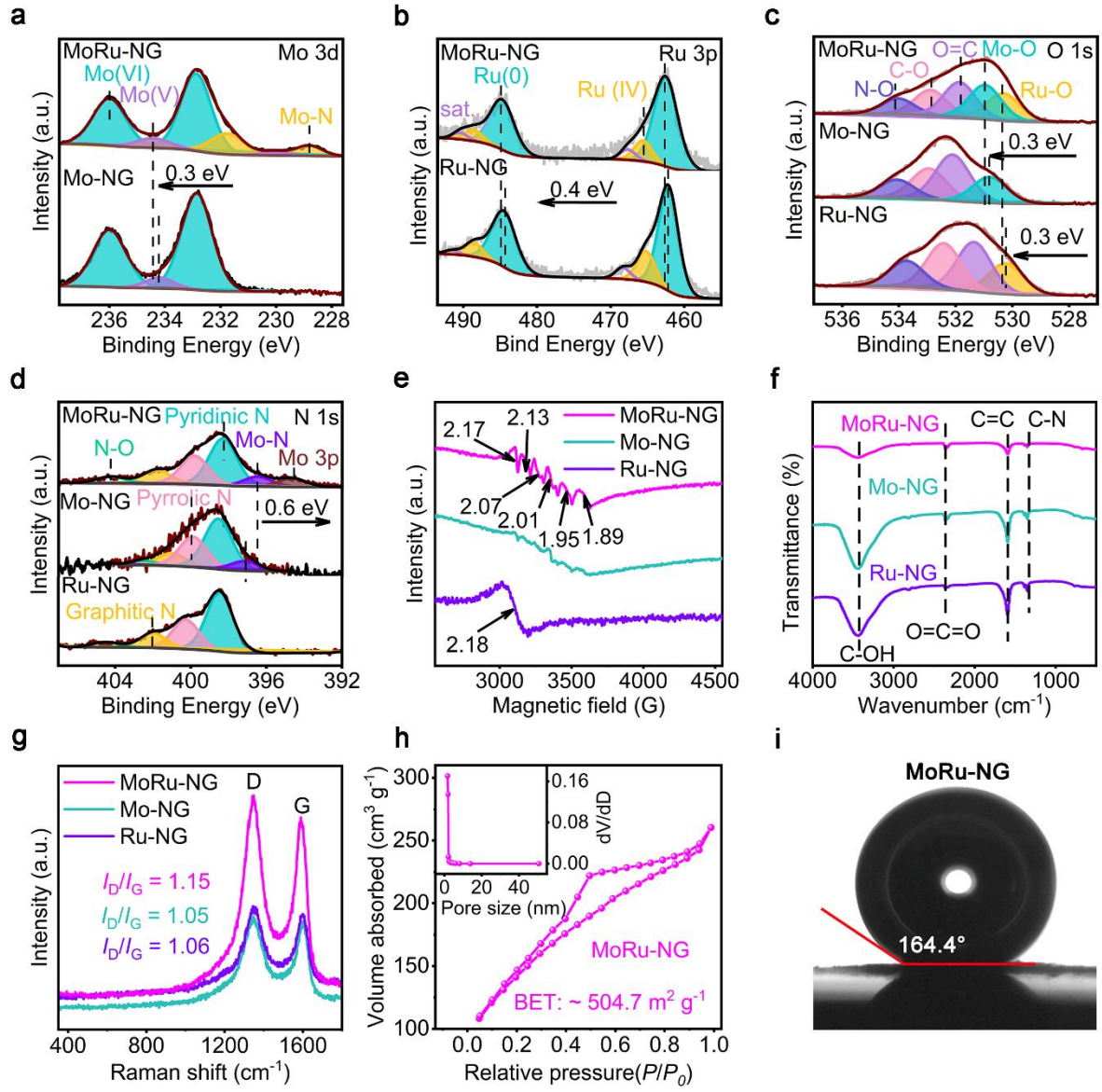

Figure 3. The high-resolution XPS spectra of (a) Mo 3d, (b) Ru 3p, (c) O 1s, and (d) N 1s. (e) EPR spectra, (f) FTIR spectra, and (g) Raman spectra of MoRu-NG, Mo-NG, Ru-NG. (h) N_2 adsorption-desorption isotherm of MoRu-NG; the inset is pore size distribution diagram. (i) Air bubble CA of MoRu-NG.

Moreover, the comparison samples with various mass percentage of Mo atoms relative to Ru atoms were also characterized via XPS measurements. For Mo 3d and Ru 3p spectra, the varying mass percentage of Mo atoms relative to Ru atoms catalyzes an electron migration at a specific Mo loading (**Figure S7** and **S8**). For N 1s spectrum, pyridinic N (398.3 eV), pyrrolic N (399.8 eV), graphitic N (401.7 eV), and N–O (404.3 eV) species can be clearly visible in all catalysts while Mo-N (394.6 eV) only appears in MoRu-NG and Mo-NG, demonstrating Mo atoms coordinating with N atoms (**Figure**

 doi:10.20944/preprints202503.1578.v1

3d). Compared to Mo-NG, a negative shift of 0.6 eV is observed on Mo–N in MoRu-NG, exhibiting electron density increase around Mo–N bonds, confirming that electron transfer exists between Mo–Ru NPAs and NG sheets. For O 1s and N 1s spectra, N–O bonds disappear while Mo loading gradually increases to the certain values, representing that excessive Mo loading effects the formation of N–O bonds (**Figure S9** and **S10**). Meanwhile, the C 1s spectra are resolved into four characteristic peaks, corresponding to C–C (284.8 eV), C–N (285.6 eV), C–O (286.4 eV), and O=C–O (287.3 eV) species (**Figure S11** and **S12**), which represents that N atoms have a coordination relationship with C atoms. Distinctly, the metal centers in MoRu-NG are O-coordinated, while Mo SAs in Mo–Ru NPAs are anchored in NG with Mo–N–C structure.

The electron paramilitary resonance spectroscopy (EPR) was used to solve MoRu-NG surface defects (**Figure 3e**). The signals of g = 2.17 and g = 2.13 are assigned to the resonance on conduction electrons in MoRu-NG [32]. MoRu-NG and Mo-NG both display the EPR signals at g = 1.95 (Mo–N species [33]), g = 1.89 and g = 2.07 (Mo^{5+} species [34]), followed by g = 2.01 (oxygen vacancies), suggesting that MoRu-NG has higher concentration about O_v, Mo^{5+} and Mo–N species than that of Mo-NG. Moreover, the reference samples with heterogeneous mass percentage of Mo atoms relative to Ru atoms display analogous EPR spectra compared with MoRu-NG in the **Figure S13**. As Mo loading increases gradually, the signal intensity is more and more obvious, demonstrating that the concentration of free radicals is related to Mo loading. In order to identify the varieties of chemical groups, Fourier transform infrared spectroscopy (FT-IR) was conducted. The FT-IR spectra of MoRu-NG include the vibration of C–OH, O=C=O, C=C and C–N groups in **Figure 3f**. Compared with MoRu-NG, the control samples with various atom mass ratios exhibit similar characteristic bands (**Figure S14**). As exhibited in Raman spectra, the intensity ratio of D band to G band (ID/IG) for MoRu-NG (1.15) is higher than those of Mo-NG (1.05) and Ru-NG (1.06) (**Figure 3g**). This result indicates that structural defect is introduced into MoRu-NG via synergistic effect between Mo and Ru atoms. In addition, ID/IG for MoRu-NG (1.15) is higher than those of A-MR (1.05) and C-MR (1.02), which demonstrates that adjusting atom mass ratio to appropriate values can introduce more structural defects (**Figure S15**).

Moreover, MoRu-NG affords a higher air contact angle (CA, 164.4°) and water contact angle (CA, 115.7°) than those of Mo-NG and Ru-NG, signifying the hydrophobic, which promotes the diffusion of hydrogen gas (**Figure 3I**, **Figure S16** and **S17**). Furthermore, the Brunauer-Emmett-Teller (BET) surface areas of MoRu-NG, Mo-NG and Ru-NG are 504.7, 237.1 and 150 $m^2\ g^{-1}$, respectively, and the main pore size of MoRu-NG is centered at 1.6 nm (**Figure 3h**, **Figure S18** and **S19**). The results suggest that introducing Mo SAs into Ru crystals can effectively inhibit the agglomeration of Ru atoms during CVD process. Inserting Mo atoms into Ru lattices generates a considerable amount of holes and defects, which contributes to the adsorption of reactant molecules and increases the number of accessible active sites [35].

In this work, $RuMo_3$ groups are synthesized with Ru–O–Mo configuration through facile self-assembly of Mo species and Ru species, followed by CVD procedure. Usually, SAs about transition metals are spread over N-doped carbon support as M–N–C structures (M refers to transition metals). Therefore, Mo SAs in $RuMo_3$ groups were dispersed on N-doped carbon support with the form of Mo–N–C in the CVD procedure [36,37]. In MoRu-NG, O, O'-bidentate ligands and chelation function between Mo and Ru atoms provide the possibility to modulate electronic structure, thereby improving electrocatalytic activity and stability.

3.3. Electrocatalytic HER Performance

The electrocatalytic hydrogen evolution reaction (HER) performance of MoRu-NG was explored in 0.5 M H_2SO_4, 1.0 M KOH, and 1.0 M PBS seawater solutions by utilizing a three-electrode configuration. For the purpose of comparison, Mo-NG, Ru-NG, NG, and commercial Pt/C were also tested. In this study, all the potentials are based on a reversible hydrogen electrode (RHE), and it should be noted that all the data obtained are without IR compensation.

 doi:10.20944/preprints202503.1578.v1

In 0.5 M H_2SO_4 seawater solution, MoRu-NG has the ability to provide a geometric current density of –10 mA cm^{-2} at an extraordinarily low overpotential of 53 mV (η_{10} = 53 mV) (**Figure 4a**). This overpotential is significantly lower than those of NG (>300 mV), Mo-NG (292 mV), and Ru-NG (153 mV), as well as other counterparts (**Figure S20**), suggesting that MoRu-NG serves as a first rate HER catalyst. In order to acquire more profound knowledge about the reaction kinetics of MoRu-NG, the Tafel slope was scrutinized. In 0.5 M H_2SO_4 seawater solution, MoRu-NG delivers a small Tafel slope of 30 mV dec^{-1}, which is far lower than those of NG (183 mV dec^{-1}), Mo-NG (162 mV dec^{-1}), Ru-NG (139 mV dec^{-1}), and other counterparts, as well as close to that of the benchmark Pt/C (30 mV dec^{-1}) (**Figure 4b**, **Figure S20**). The results reflect that MoRu-NG has the top-level HER kinetic process in accordance with the Volmer-Tafel mechanism, where the surface recombination step belongs to the rate-limiting step. Compared to Mo-NG, Ru-NG, NG and Pt/C, MoRu-NG shows the best activity, featuring high current density at low overpotential in 1.0 M KOH seawater solution (**Figure 4c**). MoRu-NG merely requires overpotentials of 28 mV to reach –10 mA cm^{-2}, which is lower than those of Mo-NG (290 mV), Ru-NG (270 mV), NG (>300mV), and other catalysts of different atom mass ratios, as well as even better than that of the state-of-the-art Pt/C (37 mV) (**Figure S20**). In a corresponding fashion, the reaction kinetics within MoRu-NG undergoes a great leap forward, which is demonstrated by the unusually low Tafel slope of 37 mV dec^{-1} observed in the 1.0 M KOH seawater solution (**Figure 4d**). The Tafel slope (37 mV dec^{-1}) of MoRu-NG is superior to those of Mo-NG (128 mV dec^{-1}), Ru-NG (133 mV dec^{-1}), NG (140 mV dec^{-1}), and other catalysts of different atom mass ratios, as well as close to that of the commercial Pt/C (34 mV dec^{-1}) (**Figure S20**). In 1.0 M KOH seawater solution, such a low Tafel slope of MoRu-NG suggests that the introduction of Mo SAs favors the generation of H* from H_2O. In 1.0 M PBS seawater solution, MoRu-NG shows the optimal activity, characterized by high current density even at low overpotential and small Tafel slope compared to Mo-NG, Ru-NG, NG and Pt/C (**Figure S21**).

 doi:10.20944/preprints202503.1578.v1

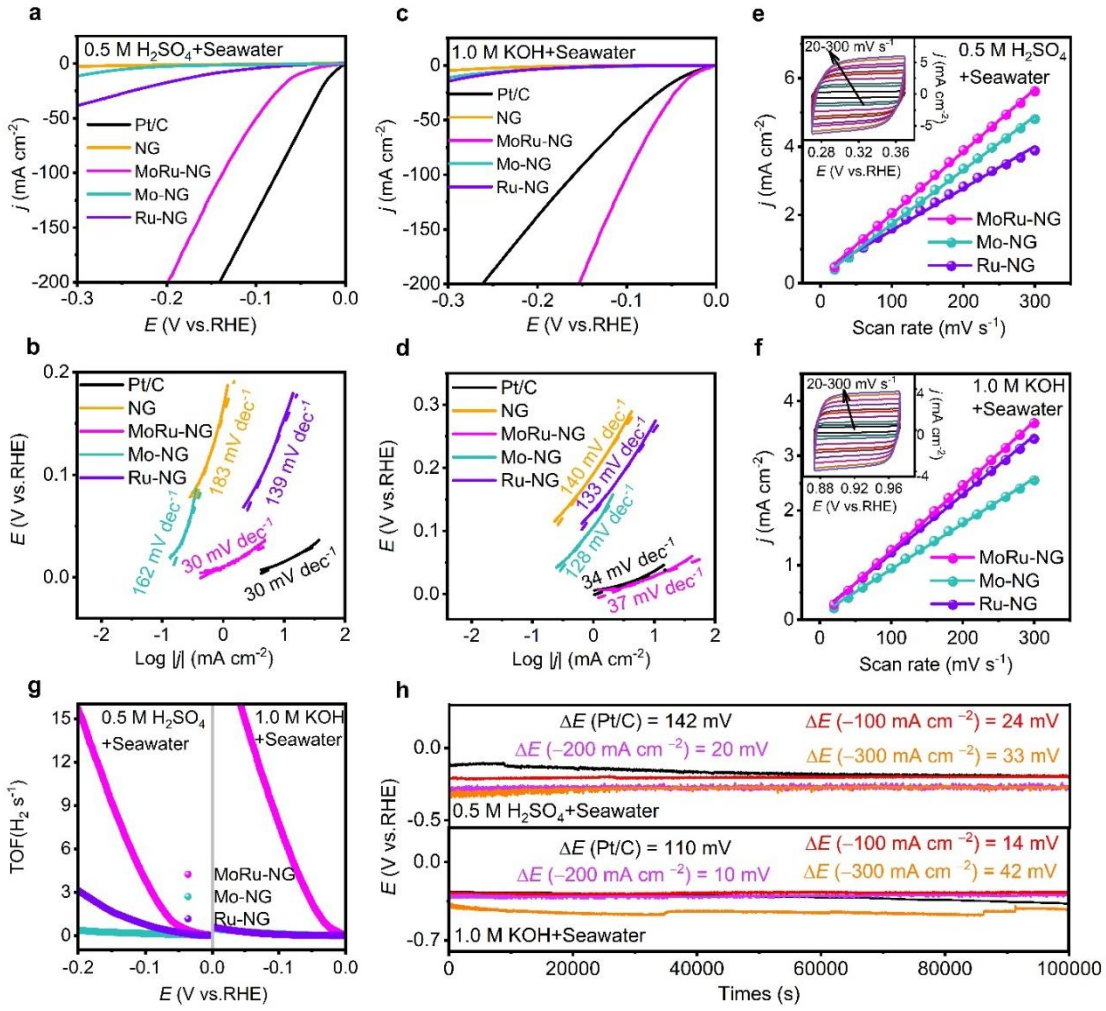

Figure 4. The Polarization curves and the corresponding Tafel plots of MoRu-NG, Mo-NG, Ru-NG, NG, and Pt/C in (a and b) 0.5 M H_2SO_4 and (c and d) 1.0 M KOH seawater solutions, respectively. C_{dl} measurement with varying scan rates from 20 to 300 mV s^{-1} in (e) 0.5 M H_2SO_4 and (f) 1.0 M KOH seawater solutions, respectively; inset is CV cycle of MoRu-NG. (g) TOF values of MoRu-NG, Mo-NG, and Ru-NG in 0.5 M H_2SO_4 (left) and 1.0 M KOH (right) seawater solutions, respectively. (h) Galvanostatic measurement of MoRu-NG in 0.5 M H_2SO_4 and 1.0 M KOH at j = –100, –200, and –300 mA cm^{-2}, respectively.

In addition, the technology of double-layer electrochemical capacity (C_{dl}) at different scanning rates by cyclic voltammetry (CV) was applied. In 0.5 M H_2SO_4 and 1.0 M KOH seawater solutions, MoRu-NG has the C_{dl} values of 18.3 and 11.8 mF cm^{-2}, respectively. These values are higher than those of Mo-NG (15.8 and 8.3 mF cm^{-2}) and Ru-NG (12.3 and 10.8 mF cm^{-2}) (**Figure 4e** and **Figure 4f**, **Figure S22**). The result suggests that the chelation function between Mo and Ru atoms can subjoin active surface areas of catalysts. Another point is that the C_{dl} values for MoRu-NG (18.3, 11.8 mF cm^{-2}) are higher than those of NG (7.61, 5.2 mF cm^{-2}), A-MR (15.8, 6.0 mF cm^{-2}) and C-MR (11.2, 9.0 mF cm^{-2}) in 0.5 M H_2SO_4 and 1.0 M KOH seawater solutions, respectively (**Figure S23** and **S24**). This result demonstrates that deficient and overly high Mo loading both reduce the number of accessible active sites, indicating that electrochemical activity depends on rational Mo content [38,39]. By using pure water to formulate acidic and basic solution, the polarization curves along with their respective Tafel plots of MoRu-NG are shown in the **Figure S25**. In the same way, MoRu-NG has the C_{dl} values of 13.2 and 9.6 mF cm^{-2} in 0.5 M H_2SO_4 and 1.0 M KOH pure water solutions, respectively, which are similar to that of MoRu-NG in acidic and alkaline seawater solutions **(Figure S26)**. The results explain that MoRu-NG can resist poison and erosion about anions and cations in seawater compared with

 doi:10.20944/preprints202503.1578.v1

pure water [40], which can prevent the wastage of fresh water and enhance the utilization efficiency of seawater.

To research the intrinsic catalytic activity, the electrochemical surface area (ECSA) determined by deriving the electrochemical double-layer capacitance (C_{dl}) was measured. The ECSA of MoRu-NG, Mo-NG and Ru-NG are 457.5, 395.0, and 307.5 cm^2 in 0.5 M H_2SO_4 seawater solution, and 295.0, 207.5, and 270.0 cm^2 in 1.0 M KOH seawater solutions, respectively. Additionally, to exclude the effect of surface area and compare the inherent HER activity, geometric current density (j) was normalized by ECSA (j_{ECSA}) in the pH-universal seawater [41,42]. As shown in **Figure S27**, MoRu-NG gives the j_{ECSA} values of 110.0 and 341.7 μA cm^{-2} at η = 100 mV, which are evidently higher than those of Mo-NG (2.7, 4.2 μA cm^{-2}) and Ru-NG (14.1, 1.8 μA cm^{-2}) in 0.5 M H_2SO_4 and 1.0 M KOH seawater solutions, respectively. The outcome reveals that MoRu-NG possesses better intrinsic HER activity than those of Mo-NG and Ru-NG in 0.5 M H_2SO_4 and 1.0 M KOH seawater solutions, respectively. For the sake of an uncomplicated comparison, the η_{10} and Tafel slope values of MoRu-NG are further compared with other recently reported Mo or Ru based metal electrocatalysts (**Figure S28** and **S29**, **Table S3** and **S4**). The small η_{10} and Tafel slope of MoRu-NG are competitive with these electrocatalysts, such as Ni_2P/MoS_2/N:CNT [43] and CoRu-1 [44] and other catalysts [45–60], suggesting that MoRu-NG is a top HER electrocatalyst in the pH-universal seawater.

In addition, in order to obtain more in-depth understanding of the intrinsic catalytic activity, the turnover frequency (TOF) per active site was determined. Thus, the number of active sites was titrated from integrated charge of anodic CV cycles at phosphate buffer solution (pH = 7) [61] (**Figure S30**). Evidently, MoRu-NG affords the highest TOF values of 3.85 and 7.8 H_2 s^{-1} at η = 100 mV, significantly surpassing those of Mo-NG (0.15 and 0.12 H_2 s^{-1}) and Ru-NG (0.76 and 0.09 H_2 s^{-1}) in 0.5 M H_2SO_4 and 1.0 M KOH seawater solutions, respectively (**Figure 4g**). These results demonstrate that MoRu-NG delivers significantly enhanced catalytic hydrogen production capacity compared to Mo-NG and Ru-NG. This superior catalytic performance in HER can be ascribed to the distinctive Ru–O–Mo–N–C configuration [62]. This configuration gives rise to a unique electronic structure and improves electrical conductivity [63]. Additionally, electrochemical impedance spectroscopy (EIS) technique was also carried out. Among them, MoRu-NG yields small charge-transfer resistance (R_{ct}) (3 and 5 ohms) in 0.5 M H_2SO_4 and 1.0 M KOH seawater solutions, which are much lower than those of Mo-NG (9 and 7 ohms), and Ru-NG (6 and 7 ohms), respectively (**Figure S31**). MoRu-NG exhibits lower R_{ct} than those of Mo-NG and Ru-NG, indicating that the atom doping of foreign metal facilitates electron transport at the electrode or electrolyte interface. The chemical coupling between Mo and Ru atoms provides an interconnected conductive network to enhance the electrical conductivity between Mo–Ru NPAs and NG sheets [64].

The following researches results are about stability and durability of MoRu-NG electrocatalysts. As illustrated in **Figure S32**, the polarization curve of MoRu-NG exhibits minimal discrepancies compared with the initial curve after 10,000 even 50,000 CV cycles in 0.5 M H_2SO_4 seawater solution. This is the case even after 10,000 or, remarkably, 50,000 cyclic voltammetry (CV) cycles in 1.0 M KOH seawater solution (**Figure S33**). Furthermore, several long-term potential stability tests were conducted on MoRu-NG using galvanostatic measurement at current densities of –100, –200, and –300 mA cm^{-2} under room temperature (25°C) (**Figure 4g**). After 100,000 s of operation at j = –100, –200, and –300 mA cm^{-2}, the potentials of MoRu-NG only increase by 24, 20, and 33 mV in 0.5 M H_2SO_4 seawater solution, and 14, 10, and 42 mV in 1.0 M KOH seawater solution, respectively. In contrast, the potentials of Pt/C catalysts at j = –100 mA cm^{-2} increase by 142 and 110 mV in 0.5 M H_2SO_4 and 1.0 M KOH seawater solutions, respectively. These outcomes demonstrate that MoRu-NG has exceptional stability and durability in acidic and alkaline electrolytes. In XRD patterns, the typical diffraction peaks of MoRu-NG still reveal Ru crystalline (PDF#06-0663) phase after electrochemical cycling (**Figure S34**). And beyond that, TEM characterization displays that Mo–Ru NPAs in MoRu-NG still maintain fine nanoparticle state after electrochemical cycling (**Figure S35**). In addition, chemical valence states of Mo and Ru species remain almost unchanged, further signifying the robustness of MoRu-NG catalysts in the electrocatalytic HER process (**Figure S36** and **S37**). The

 doi:10.20944/preprints202503.1578.v1

structure of O, O′-bidentate ligands in MoRu-NG shortens Ru–Ru bond length and provides stronger Ru metallic bonds to enhance the electrocatalytic stability [20]. In this work, the excellent physicochemical stability of MoRu-NG is attributed to the particular coordination structure between Mo and Ru atoms in NG sheets through electrostatic self-assembly [65,66].

3.4. Mechanism of HER and Schematic Representation of Seawater Electrocatalysis.

MoRu-NG has higher HER kinetic process than other electrocatalysts through the Volmer-Tafel mechanism. In fact, HER occur based on the Volmer-Heyrovsky mechanism or the Volmer-Tafel mechanism, while the evolutionary steps of HER are similar in both alkaline and acidic media (**Figure 5a**). For both acidic and alkaline conditions, the first step of HER is the Volmer reaction, which produces H* intermediates on MoRu-NG. In this work, Ru sites on MoRu-NG were chosen as active metal sites and potential adsorption sites for H* intermediates. The second step is the Rate Determination step (RDS), belonging to the surface recombination step, which indicates that the process of RDS depends on the activity of catalysts. Consequently, Pt-based catalysts undergo the Tafel reaction in order to adsorb double H* intermediates to produce H_2, while MoRu-NG as the transition metal catalyst typically reacts with H_2O (in alkaline conditions) or H^+ (in acidic conditions) to produce H_2. Schematic representation of seawater electrocatalysis is shown in the **Figure 5b**. In the actual overall seawater splitting test, the assembled MoRu-NG || RuO_2 system exhibits better performance than the commercial Pt/C || RuO_2 electrode pair (**Figure S38**). It is evident that the assembled MoRu-NG || RuO_2 system requires lower voltages to achieve the required current density compared to the commercial electrode sets, demonstrating that the catalyst has the high activity for full seawater splitting. Meanwhile, the assembled MoRu-NG electrode pairs can also operate stably for 100,000s at current density of 300 mA cm^{-2}, which indicates its good durability for full seawater splitting (**Figure S39**).

 doi:10.20944/preprints202503.1578.v1

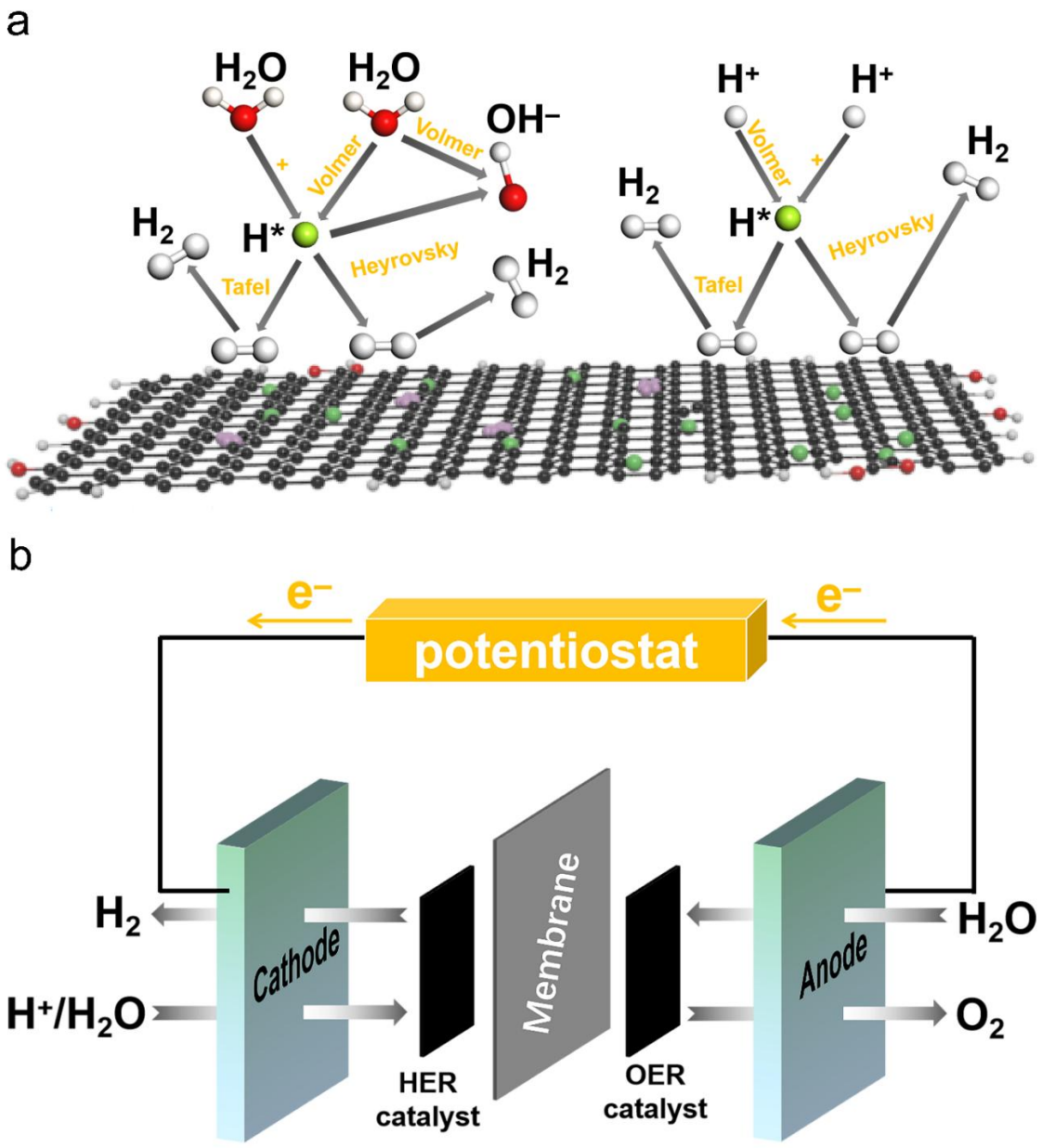

Figure 5. Mechanism of HER (a) and schematic representation (b) of seawater electrocatalysis.

Conclusion

In summary, MoRu-NG has been successfully synthesized by facile hydrothermal and CVD methods, in which Mo–Ru NPAs are O-coordinated. Additionally, MoRu-NG exhibits well-defined Ru–O–Mo–N–C structure characterized by the presence of O, O′-bidentate ligands. In MoRu-NG, Ru atoms have half full d-electron orbitals and thus possess optimal hydrogen adsorption energy, which indicates that the excellent HER activity is determined by Ru centers. The O, O′-bidentate ligands in MoRu-NG play a vital role in HER performance, shortening Ru–Ru bond length in Ru NPs, which increases Ru metallic bond intensity and further promotes HER stability. The high HER activity of MoRu-NG mainly depends on Ru atoms as the active center and the excellent HER stability is attributed to the structure of O, O′-bidentate ligands after the introduction of Mo SAs. Therefore, the pursuit of knowledge and understanding regarding strong electron coupling offer a favorable pathway for the development of cost-effective, high-performance, and durable catalysts within the renewable energy economy.

 doi:10.20944/preprints202503.1578.v1

Supplementary Materials: The following supporting information can be downloaded at the website of this paper posted on Preprints.org.

Author Contributions: Shuhan Wang: conceptualization, data curation, formal analysis, investigation, writing-review & editing; **Jiani Qin**: conceptualization, writing-review & editing, supervision, resources; **Yong Zhang**: conceptualization, writing-review & editing, supervision, resources; **Shuai Chen**: conceptualization, investigation, writing-review & editing; **Wenjun Yan**: writing-review & editing, resources; **Haiqing Zhou**: conceptualization, writing-review & editing, supervision, resources; **Xiujun Fan**: funding acquisition, writing-review & editing, project administration, resources, supervision.

Acknowledgments: The authors state that they have no recognized competing financial interests or personal connections that might seem to have affected the work presented in this paper. This research was funded by the National Natural Science Foundation of China (No. 22175109) and the "Young Talent Support Plan" of Xi'an Jiaotong University. The authors are thankful to the Instrument Analysis Center of Xi'an Jiaotong University for their help with XRD, XPS, and TEM analyses.

Conflicts of Interest: The authors declare no competing financial interests.

References

1. Z. Cai, J. Liang, Z. Li, T. Yan, C. Yang, S. Sun, M. Yue, X. Liu, T. Xie, Y. Wang, T. Li, Y. Luo, D. Zheng, Q. Liu, J. Zhao, X. Sun, B. Tang, Stabilizing NiFe sites by high-dispersity of nanosized and anionic Cr species toward durable seawater oxidation, Nature communications, 15 (2024) 6624.
2. L. Li, L. Bu, B. Huang, P. Wang, C. Shen, S. Bai, T.S. Chan, Q. Shao, Z. Hu, X. Huang, Compensating Electronic Effect Enables Fast Site-to-Site Electron Transfer over Ultrathin RuMn Nanosheet Branches toward Highly Electroactive and Stable Water Splitting, Advanced materials (Deerfield Beach, Fla.), 33 (2021) e2105308.
3. Y. Xue, L. Shi, X. Liu, J. Fang, X. Wang, B.P. Setzler, W. Zhu, Y. Yan, Z. Zhuang, A highly-active, stable and low-cost platinum-free anode catalyst based on RuNi for hydroxide exchange membrane fuel cells, Nature communications, 11 (2020) 5651.
4. Y. Zhao, X. Wang, G. Cheng, W. Luo, Phosphorus-Induced Activation of Ruthenium for Boosting Hydrogen Oxidation and Evolution Electrocatalysis, ACS Catalysis, 10 (2020) 11751-11757.
5. T. Zhao, D. Xiao, Y. Chen, X. Tang, M. Gong, S. Deng, X. Liu, J. Ma, X. Zhao, D. Wang, Boosting alkaline hydrogen electrooxidation on an unconventional fcc-Ru polycrystal, Journal of Energy Chemistry, 61 (2021) 15-22.
6. Y. Zhou, Z. Xie, J. Jiang, J. Wang, X. Song, Q. He, W. Ding, Z.J.N.C. Wei, Lattice-confined Ru clusters with high CO tolerance and activity for the hydrogen oxidation reaction, 3 (2020) 454-462.
7. W. Luo, Y. Wang, C. Cheng, Ru-based electrocatalysts for hydrogen evolution reaction: Recent research advances and perspectives, Materials Today Physics, 15 (2020) 100274.
8. F. Dionigi, T. Reier, Z. Pawolek, M. Gliech, P. Strasser, Design Criteria, Operating Conditions, and Nickel-Iron Hydroxide Catalyst Materials for Selective Seawater Electrolysis, ChemSusChem, 9 (2016) 962-972.
9. J. Li, J. Jurasz, H. Li, W.-Q. Tao, Y. Duan, J. Yan, A new indicator for a fair comparison on the energy performance of data centers, Applied Energy, 276 (2020) 115497.
10. T. Ulhaq, Y. Haik, Strategies of Anode Design for Seawater Electrolysis: Recent Development and Future Perspective, Small Science, 2 (2022).
11. H.J. Song, H. Yoon, B. Ju, D.-Y. Lee, D.-W. Kim, Electrocatalytic Selective Oxygen Evolution of Carbon-Coated $Na_2Co_{1-x}Fe_xP_2O_7$ Nanoparticles for Alkaline Seawater Electrolysis, ACS Catalysis, 10 (2020) 702-709.
12. L. Yu, Q. Zhu, S. Song, B. McElhenny, D. Wang, C. Wu, Z. Qin, J. Bao, Y. Yu, S. Chen, Z. Ren, Non-noble metal-nitride based electrocatalysts for high-performance alkaline seawater electrolysis, Nature communications, 10 (2019) 5106.
13. H. Chen, Y.-Q. Wang, R. Ding, Z.-W. Zeng, B.-W. Liu, F.-R. Zeng, Y.-Z. Wang, H.-B. Zhao, Satellite-like shielding for dual single-atom catalysis, boosting ampere-level alkaline seawater splitting, Matter, 7 (2024) 3189-3204.

 doi:10.20944/preprints202503.1578.v1

14. X. Kang, F. Yang, Z. Zhang, H. Liu, S. Ge, S. Hu, S. Li, Y. Luo, Q. Yu, Z. Liu, Q. Wang, W. Ren, C. Sun, H.M. Cheng, B. Liu, A corrosion-resistant RuMoNi catalyst for efficient and long-lasting seawater oxidation and anion exchange membrane electrolyzer, Nature communications, 14 (2023) 3607.
15. Y. Huang, Y. Sun, X. Zheng, T. Aoki, B. Pattengale, J. Huang, X. He, W. Bian, S. Younan, N. Williams, J. Hu, J. Ge, N. Pu, X. Yan, X. Pan, L. Zhang, Y. Wei, J. Gu, Atomically engineering activation sites onto metallic 1T-MoS(2) catalysts for enhanced electrochemical hydrogen evolution, Nature communications, 10 (2019) 982.
16. J. Zhao, R. Urrego-Ortiz, N. Liao, F. Calle-Vallejo, J. Luo, Rationally designed Ru catalysts supported on TiN for highly efficient and stable hydrogen evolution in alkaline conditions, Nature communications, 15 (2024) 6391.
17. L.R. Radovic, B. Bockrath, On the Chemical Nature of Graphene Edges: Origin of Stability and Potential for Magnetism in Carbon Materials, Journal of the American Chemical Society, 127 (2005) 5917-5927.
18. G. Zhang, J. Pei, Y. Wang, G. Wang, Y. Wang, W. Liu, J. Xu, P. An, H. Huang, L. Zheng, S. Chu, J. Dong, J. Zhang, Selective Activation of Lattice Oxygen Site Through Coordination Engineering to Boost the Activity and Stability of Oxygen Evolution Reaction, Angewandte Chemie International Edition, 63 (2024) e202407509.
19. A. Müller, F. Peters, M.T. Pope, D. Gatteschi, Polyoxometalates: Very Large ClustersNanoscale Magnets, Chemical Reviews, 98 (1998) 239-272.
20. Y. Chen, Y. Liu, L. Li, T. Sakthivel, Z. Guo, Z. Dai, Intensifying the Supported Ruthenium Metallic Bond to Boost the Interfacial Hydrogen Spillover Toward pH-Universal Hydrogen Evolution Catalysis, Advanced Functional Materials, 34 (2024).
21. R. Maji, S.C. Mallojjala, S.E. Wheeler, Electrostatic Interactions in Asymmetric Organocatalysis, Accounts of Chemical Research, 56 (2023) 1990-2000.
22. J. Yi, S. Zhan, L. Chen, Q. Tian, N. Wang, J. Li, W. Xu, B. Zhang, M.S.G. Ahlquist, Electrostatic Interactions Accelerating Water Oxidation Catalysis via Intercatalyst O–O Coupling, Journal of the American Chemical Society, 143 (2021) 2484-2490.
23. X.L. Xu, N.N. Wang, Y.H. Zou, X. Qin, P. Wang, X.Y. Lu, X.Y. Zhang, W.Y. Sun, Y. Lu, N, N′-bidentate ligand anchored palladium catalysts on MOFs for efficient Heck reaction, Nature communications, 15 (2024) 7273.
24. Y. Yun, H. Zeng, L. Li, H. Li, S. Cheng, N. Sun, M. Li, H. Sheng, S. Hu, T. Yao, M. Zhu, Matching Bidentate Ligand Anchoring: an Accurate Control Strategy for Stable Single-Atom/ZIF Nanocatalysts, Advanced materials (Deerfield Beach, Fla.), 35 (2023) e2209561.
25. W. Sun, T. Kuang, G. Wei, Y. Li, Y. Liu, S. Lyu, Y. Zhang, J. Li, L.J.N.R. Wang, Design and construction of size-controlled CoO/CS catalysts for Fischer–Tropsch synthesis, (2023).
26. L. Gao, H. Wang, F. Meng, H. Peng, X. Lyu, M. Zhu, Y. Wang, C. Lu, J. Liu, T. Lin, A. Ji, L. Gu, P. Yu, S. Meng, Z. Cao, N. Lu, Unveiling Strong Ion–Electron–Lattice Coupling and Electronic Antidoping in Hydrogenated Perovskite Nickelate, Advanced materials (Deerfield Beach, Fla.), 35 (2023) e2300617.
27. H.X. Liu, J.Y. Li, X. Qin, C. Ma, W.W. Wang, K. Xu, H. Yan, D. Xiao, C.J. Jia, Q. Fu, D. Ma, Pt(n)-O(v) synergistic sites on MoO(x)/γ-Mo(2)N heterostructure for low-temperature reverse water-gas shift reaction, Nature communications, 13 (2022) 5800.
28. Z. Zhao, J. Sun, X. Li, S. Qin, C. Li, Z. Zhang, Z. Li, X. Meng, Engineering active and robust alloy-based electrocatalyst by rapid Joule-heating toward ampere-level hydrogen evolution, Nature communications, 15 (2024) 7475.
29. Z. Wang, W. Xu, G. Tan, X. Duan, B. Yuan, M.G. Sendeku, H. Liu, T. Li, F. Wang, Y. Kuang, X. Sun, Single atomic Ru in TiO_2 boost efficient electrocatalytic water oxidation to hydrogen peroxide, Science Bulletin, 68 (2023) 613-621.
30. Y. Wang, Y. Wen, Y. Cheng, X. Chen, M. Zhuansun, T. Wang, J. Li, D. Meira, H. Sun, J. Wei, J. Zhou, Y. Wang, S. He, Enriched electrophilic oxygen species facilitate acidic oxygen evolution on Ru-Mo binary oxide catalysts, Nano Research, 17 (2023).

 doi:10.20944/preprints202503.1578.v1

31. H. Shi, Y. Yang, P. Meng, J. Yang, W. Zheng, P. Wang, Y. Zhang, X. Chen, Z. Cheng, C. Zong, D. Wang, Q. Chen, Local Charge Transfer Unveils Antideactivation of Ru at High Potentials for the Alkaline Hydrogen Oxidation Reaction, Journal of the American Chemical Society, 146 (2024) 16619-16629.
32. N. Taratanov, G. Yurkov, A. Fionov, Y. Koksharov, O. Popkov, V. Kolesov, Creation and physical properties of the molybdenum-containing polyethylene-based nanomaterials, Journal of Communications Technology and Electronics - J COMMUN TECHNOL ELECTRON, 54 (2009) 937-946.
33. K. Zhang, G. Zhang, J. Qu, H. Liu, Tungsten-Assisted Phase Tuning of Molybdenum Carbide for Efficient Electrocatalytic Hydrogen Evolution, ACS Applied Materials & Interfaces, 10 (2018) 2451-2459.
34. D. Ma, Y. Shu, X. Bao, Y. Xu, Methane Dehydro-aromatization under Nonoxidative Conditions over Mo/HZSM-5 Catalysts: EPR Study of the Mo Species on/in the HZSM-5 Zeolite, Journal of Catalysis, 189 (2000) 314-325.
35. H.-W. Liang, W. Wei, Z.-S. Wu, X. Feng, K. Müllen, Mesoporous Metal–Nitrogen-Doped Carbon Electrocatalysts for Highly Efficient Oxygen Reduction Reaction, Journal of the American Chemical Society, 135 (2013) 16002-16005.
36. K. Ye, M. Hu, Q.-K. Li, Y. Han, Y. Luo, J. Jiang, G. Zhang, Cooperative Nitrogen Activation and Ammonia Synthesis on Densely Monodispersed Mo–N–C Sites, The Journal of Physical Chemistry Letters, 11 (2020) 3962-3968.
37. L. Li, H. Xuan, J. Wang, X. Liang, Y. Li, Z. Han, L. Cheng, Nanoporous nonprecious multi-metal alloys as multisite electrocatalysts for efficient overall water splitting, International Journal of Hydrogen Energy, 97 (2025) 38-45.
38. L. Li, P. Li, W. Tan, K. Ma, W. Zou, C. Tang, L. Dong, Enhanced low-temperature NH_3-SCR performance of $CeTiO_x$ catalyst via surface Mo modification, Chinese Journal of Catalysis, 41 (2020) 364-373.
39. S. Cao, Z. Guan, Y. Ma, B. Xu, J. Ma, W. Chu, R. Zhang, G. Giambastiani, Y. Liu, Synergizing Mon Clusters and Mo_2C Nanoparticles on Oxidized Carbon Nanotubes Boosting the CO_2 Reduction Activity, ACS Catalysis, 14 (2024) 10939-10950.
40. H. Li, Z. Zhang, Y. Deng, F. Xu, J. Hu, D. Zhu, Q. Yu, C. Shi, Geopolymer composites for marine application: Structural properties and durability, Cement and Concrete Composites, 152 (2024) 105647.
41. J. Duan, S. Chen, C.A. Ortíz-Ledón, M. Jaroniec, S.Z.J.A.C.I.E. Qiao, Phosphorus Vacancies that Boost Electrocatalytic Hydrogen Evolution by Two Orders of Magnitude, (2020).
42. L. Zhang, Q. Xu, S. Wen, H. Zhang, L. Chen, H. Jiang, C. Li, Recycling Spent Ternary Cathodes to Oxygen Evolution Catalysts for Pure Water Anion-Exchange Membrane Electrolysis, ACS Nano, 18 (2024) 22454-22464.
43. M. Kim, M. Anjum, M. Lee, B.-J. Lee, J. Lee, Activating MoS_2 Basal Plane with Ni_2P Nanoparticles for Pt-Like Hydrogen Evolution Reaction in Acidic Media, Advanced Functional Materials, 29 (2019).
44. J. Jiao, N. Zhang, C. Zhang, N. Sun, Y. Pan, C. Chen, J. Li, M.-Y. Tan, R. Cui, Z. Shi, J. Zhang, H. Xiao, T.J.A.S. Lu, Doping Ruthenium into Metal Matrix for Promoted pH-Universal Hydrogen Evolution, 9 (2022).
45. P. Xiao, M.A. Sk, L.Y.P. Thia, X. Ge, R.J. Lim, J.Y. Wang, K.H. Lim, X.J.E. Wang, E. Science, Molybdenum phosphide as an efficient electrocatalyst for the hydrogen evolution reaction, 7 (2014) 2624-2629.
46. J. Zhang, R. Cui, X.a. Li, X. Liu, W. Huang, W.J.J.o.M.C. Huang, A nanohybrid consisting of NiPS3 nanoparticles coupled with defective graphene as a pH-universal electrocatalyst for efficient hydrogen evolution, 5 (2017) 23536-23542.
47. X. Geng, W. Sun, W. Wu, B. Chen, A. Al-Hilo, M. Benamara, H. Zhu, F. Watanabe, J. Cui, T.-p. Chen, Pure and stable metallic phase molybdenum disulfide nanosheets for hydrogen evolution reaction, Nature Communications, 7 (2016) 10672.
48. D.J. Li, U.N. Maiti, J. Lim, D.S. Choi, W.J. Lee, Y. Oh, G.Y. Lee, S.O. Kim, Molybdenum Sulfide/N-Doped CNT Forest Hybrid Catalysts for High-Performance Hydrogen Evolution Reaction, Nano Letters, 14 (2014) 1228-1233.
49. L. Bai, Z. Duan, X. Wen, R. Si, Q. Zhang, J. Guan, Highly Dispersed Ruthenium-Based Multifunctional Electrocatalyst, ACS Catalysis, 9 (2019) 9897-9904.

 doi:10.20944/preprints202503.1578.v1

50. Y. Xu, X. Gao, J. Zhang, D. Gao, Nitrogen-doped RuS(2) nanoparticles containing in situ reduced Ru as an efficient electrocatalyst for hydrogen evolution, RSC advances, 10 (2020) 17862-17868.
51. Q. Chen, K. Wang, J. Qin, S. Wang, W. Wei, J. Wang, Q. Shen, P. Qu, D. Liu, Ru (x) Se@MoS(2) hybrid as a highly efficient electrocatalyst toward hydrogen evolution reaction, RSC advances, 9 (2019) 13486-13493.
52. H. Lin, H. Li, Y. Li, J. Liu, X. Wang, L.J.J.o.M.C. Wang, Hierarchical CoS/MoS2 and Co3S4/MoS2/Ni2P nanotubes for efficient electrocatalytic hydrogen evolution in alkaline media, 5 (2017) 25410-25419.
53. J. Zhang, T. Wang, D. Pohl, B. Rellinghaus, R. Dong, S. Liu, X. Zhuang, X. Feng, Interface Engineering of MoS2 /Ni3 S2 Heterostructures for Highly Enhanced Electrochemical Overall-Water-Splitting Activity, Angewandte Chemie (International ed. in English), 55 (2016) 6702-6707.
54. D. Das, S. Santra, K.K. Nanda, In Situ Fabrication of a Nickel/Molybdenum Carbide-Anchored N-Doped Graphene/CNT Hybrid: An Efficient (Pre)catalyst for OER and HER, ACS Applied Materials & Interfaces, 10 (2018) 35025-35038.
55. H. Song, M. Wu, Z. Tang, J.S. Tse, B. Yang, S. Lu, Single Atom Ruthenium-Doped CoP/CDs Nanosheets via Splicing of Carbon-Dots for Robust Hydrogen Production, Angewandte Chemie (International ed. in English), 60 (2021) 7234-7244.
56. A. Jiang, Z. Wang, Q. Li, M. Dong, An efficient ruthenium-based dual-electrocatalyst towards hydrogen evolution and oxygen reduction reactions, Materials Today Physics, 16 (2021) 100300.
57. G. Li, K. Zheng, W. Li, Y. He, C. Xu, Ultralow Ru-Induced Bimetal Electrocatalysts with a Ru-Enriched and Mixed-Valence Surface Anchored on a Hollow Carbon Matrix for Oxygen Reduction and Water Splitting, ACS Appl Mater Interfaces, 12 (2020) 51437-51447.
58. W. Li, Z. Wei, B. Wang, Y. Liu, H. Song, Z. Tang, B. Yang, S. Lu, Carbon quantum dots enhanced the activity for the hydrogen evolution reaction in ruthenium-based electrocatalysts, Materials Chemistry Frontiers, 4 (2019).
59. H. Shi, L. Liu, Y. Shi, F. Liao, Y. Li, M. Shao, Silicon monoxide assisted synthesis of Ru modified carbon nanocomposites as high mass activity electrocatalysts for hydrogen evolution, International Journal of Hydrogen Energy, 44 (2019) 11817-11823.
60. W. Wang, Y. Shao, Z. Wang, Z. Yang, Z. Zhen, Z. Zhang, C. Mao, X. Guo, G. Li, Synthesis of Ru-Doped VN by a Soft-Urea Pathway as an Efficient Catalyst for Hydrogen Evolution, ChemElectroChem, 7 (2020) 1201-1206.
61. M. Anjum, H.Y. Jeong, M. Lee, H. Shin, J.S. Lee, Efficient Hydrogen Evolution Reaction Catalysis in Alkaline Media by All-in-One MoS_2 with Multifunctional Active Sites, Advanced Materials, 30 (2017).
62. M. Li, P. Yang, W. Lv, Q. Liu, Y. Wu, S. Du, G. Huang, Z. Jiang, J. Wang, Y. Xu, Y. Zhou, S. Lu, L. Tao, S. Wang, Ultrastable Ruthenium-Based Electrocatalysts for Hydrogen Oxidation Reaction in High-Temperature Polymer Electrolyte Membrane Fuel Cells, CCS Chemistry, 0 (2024) 1-9.
63. S. Zhang, R. Ren, J. Cao, D. Zhang, J. Bai, C. Han, X. Li, L. Zhuang, P. Song, W. Xu, Ru-MnO Heterostructure Clusters Toward Efficient and CO-Tolerant Alkaline Hydrogen Oxidation Reaction, Advanced Energy Materials, (2024).
64. S. Lu, Z. Zhang, C. Chuanqi, B. Zhang, Y. Shi, Unveiling the Aggregation of M−N−C Single Atoms into Highly Efficient MOOH Nanoclusters during Alkaline Water Oxidation, Angewandte Chemie, (2024).
65. L. Wang, Z. Wei, Z. Sun, L. Zhu, Y. Gao, W. Chen, S. Li, Z.J.J.o.M.C.A. Chen, Carbon-Based Double-Metal-Site Catalysts: Advances in Synthesis and Energy Applications, (2024).
66. H. Wang, R. Niu, J. Liu, S. Guo, Y. Yang, Z. Liu, J. Li, Electrostatic self-assembly of 2D/2D $CoWO_4$/g-C_3N_4 p–n heterojunction for improved photocatalytic hydrogen evolution: Built-in electric field modulated charge separation and mechanism unveiling, Nano Research, 15 (2022) 6987-6998.